JOURNAL OF MATERIALS SCIENCE 28 (1993) 1648–1654

Monitoring the micromechanics of reinforcement in carbon fibre/epoxy resin systems

N. MELANITIS, C. GALIOTIS*, P. L. TETLOW, C. K. L. DAVIES
Materials Department, Queen Mary and Westfield College, University of London, Mile End Road, London E1 4NS, UK

The technique of laser Raman spectroscopy (LRS) was employed to obtain the interfacial shear stress (ISS) distribution along a short high-modulus carbon fibre embedded in epoxy resin at different levels of applied stress. Up to 0.6% applied strain, the ISS reached a maximum at the bonded fibre ends and decayed to zero at the middle of the fibre. At higher applied strains, the maximum value of the ISS distribution shifted away from the fibre ends towards the middle of the fibre. At the point of fibre fracture, fibre/matrix debonding was found to initiate at the fibre breaks. Further increase of applied strain resulted also in debonding initiation at the fibre ends. Current analytical stress-transfer models are reviewed in the light of the experimental data.

---

1. Introduction

1.1. Interfacial studies on carbon fibre/epoxy resin systems

Laser Raman spectroscopy (LRS) has been successfully employed recently to study the stress-transfer characteristics in carbon fibre/epoxy [1, 2], as well as aramid/epoxy systems [3, 4]. The basic principle of this technique is the fact that the Raman lines of almost all reinforcing fibres exhibit distinct and reproducible shifts when they are subjected to an external load in the fibre direction [5]. This provides unique Raman frequency versus strain calibration curves which can be used in a composite situation to convert the Raman frequencies obtained along a fibre into values of axial strain [1–5]. Furthermore, the fibre strain distribution in single-fibre model composites can be converted to an interfacial shear stress distribution via a straightforward balance-of-forces argument [1–6].

Much work has been done recently using LRS to monitor fragmentation processes in carbon fibre/epoxy resin systems [1, 2] and to review the suitability of the so-called "fragmentation test" [9, 10], as a valid test for measuring the interfacial shear strength (IFSS) of single-fibre model composites. Because the stress-transfer mechanism is activated at the locus of discontinuities, such as fibre ends or breaks, these continuous fibre model composites can only provide information about the stress state at the interface at applied strains higher than the fracture strain of the fibre. This can be a serious drawback in cases where the interfacial interactions at low strains similar to those encountered in practical composite applications, need be investigated.

Another important issue which has been raised by the previous LRS interfacial studies on continuous fibre/epoxy resin coupons [1, 2], concerns the exact location of the ISS maximum value. It has been demonstrated that in the case of a high-modulus fibre, even at applied strain of 0.8% when the first fibre fracture occurred, the maximum ISS appears at about 16 fibre diameters away from the fibre fractured end [1]. This zone of partial debonded/yielded interphase cannot be accounted for by any of the elastic stress-transfer models [11–13], not even by those that predict zero shear stresses at the very tip of the fibre due to the presence of a shear-free surface at the fibre break [14–16]. The discontinuous fibre model composite employed here is an ideal coupon geometry for monitoring the development of this zone of partial interphasial debonding/yielding at applied strains preceding fibre fracture.

Finally, the work on continuous carbon fibre/epoxy systems [1, 2] has shown that fibre/matrix debonding always accompanies fibre fracture and the propagation of debonding is driven by the strain energy of the fractured fragments. Fragmentation studies, however, cannot provide information regarding (a) the initiation of the debonding process and (b) as to whether Mode II interfacial debonding "precedes" fibre fracture or is the result of it. An attempt to answer these questions based on evidence gathered from the stress-transfer characteristics of the short carbon fibre/epoxy system, can be found here.

---

*Author to whom all correspondence should be addressed.

0022–2461

TABLE I Material properties

	Fibre: HMS	Resin: HY-1927
Young's modulus (GPa)	390	2.5
Tensile strength (MPa)	3200	60
Tensile strain to failure (%)	0.85	5–6
Shear modulus (GPa)	–	1
Diameter (μm)	7	–

2. Experimental procedure

2.1. Materials and specimen preparation

The high-modulus (HMS) carbon fibres were supplied by Courtaulds Grafil plc and had a "standard" level of surface oxidative treatment. No specific details on the fibre surface treatment process were provided. The mechanical properties of the fibres are given in Table I.

A two-part room-temperature cured MY-HY 1927 Ciba-Geigy resin was used for the short-fibre coupons. The ratio of resin to hardener was 4:1 by weight. The specimen preparation procedure involved (a) half-filling the dog-bone mould with resin, (b) laying/aligning the 2.8 mm long carbon fibre and, finally, (c) topping up the mould with the rest of the resin. The geometry of the model composite is shown schematically in Fig. 1. The resin was allowed 7 days to cure at room temperature in accordance with the manufacturer's instructions. The use of a cold-cured resin for these specimens is preferred in order to ascertain that the fibre is free of significant thermal stresses as a result of hot-curing and subsequent cooling from elevated temperatures. The mechanical properties of the resin are also listed in Table I.

2.2. Specimen testing and Raman spectrum acquisition

The dog-bone specimen was mounted on a tensile jig by clamping both its ends between metal grips which could be pulled apart. A strain gauge was attached on the resin surface and the applied strain was derived from the electrical resistance measurements using a digital multimeter. The tensometer was secured on the experimental stage which allowed the translation of the whole specimen under the laser Raman microprobe and the acquisition of the Raman spectrum.

Raman spectra were obtained using the 514.5 nm line of an argon-ion laser. The laser beam was focused to a 2 μm spot on the fibre by means of a modified Nikon microscope. The 180° backscattered beam was collected by the same microscope objective and focused on the entrance slit of a SPEX 1877 triple monochromator. The collected light was directed to a Wright Instruments charge coupled device (CCD) detector which was employed as the photon counting system. All frequency peak values were derived by applying Lorentzian fitting routines to the raw data obtained by the CCD detector.

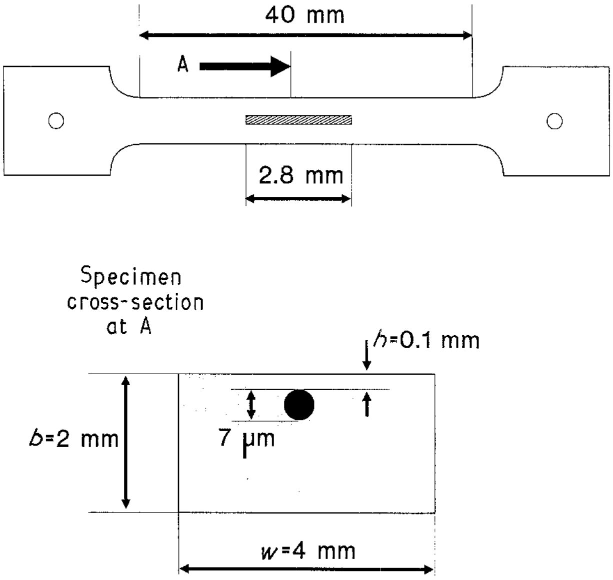

Figure 1 Short-fibre model composite specimen. The carbon fibre is located at the specimen mid-width and the strain gauge is attached to the surface of the resin block. The parameters *h*, *b*, and *w* denote distance from the free surface, thickness and width, respectively.

All measurements were conducted using a 2 μm laser spot focused at the centre of the fibre. The specimens were translated in the laser beam at intervals of 5–10 μm near a discontinuity (fibre end or break) and at larger intervals along the central region of the fibre or fragment.

3. Results

3.1. The carbon–fibre Raman spectrum and its strain dependence

The relationship between fibre Raman frequency and tensile strain is obtained by stressing a single fibre in air on a purpose-made micrometer while Raman spectra are taken at each increment of strain. As mentioned earlier, these graphs are used as the Raman frequency calibration curves for converting Raman frequency into strain in composite applications. The monitoring Raman frequency employed in the interfacial studies was the G-line, appearing at 1580 cm^{-1}. This frequency band is associated with the E_{2g} vibrational mode of the graphite crystal [17] which is the basic structural unit of carbon fibres [18, 19]. The Raman frequency shift $\Delta\nu(\varepsilon)$, induced by applied strain ε, has been found to follow, at a first approximation, a linear relationship with strain of the form [5]

$$\Delta\nu(\varepsilon) = \nu(0) - \nu(\varepsilon) = \alpha_{\varepsilon}\varepsilon \tag{1}$$

where $\nu(0)$ is the Raman frequency of the G-line at 0% applied strain, $\nu(\varepsilon)$ is the frequency value at applied strain ε, and α_{ε} is the Raman frequency gauge factor (RFGF) [5], which expresses the rate of frequency shift with strain. The graph of Raman frequency versus tensile strain for the HMS fibre is given by Melanitis *et al.* [1], p. 582, and the corresponding RFGF value has been found to be $-11.4 \pm 0.3\ \text{cm}^{-1}/(\%)$.

3.2. Strain mapping in the model composite

The strain, ε, at a point i along the embedded fibre is calculated from its corresponding Raman frequency

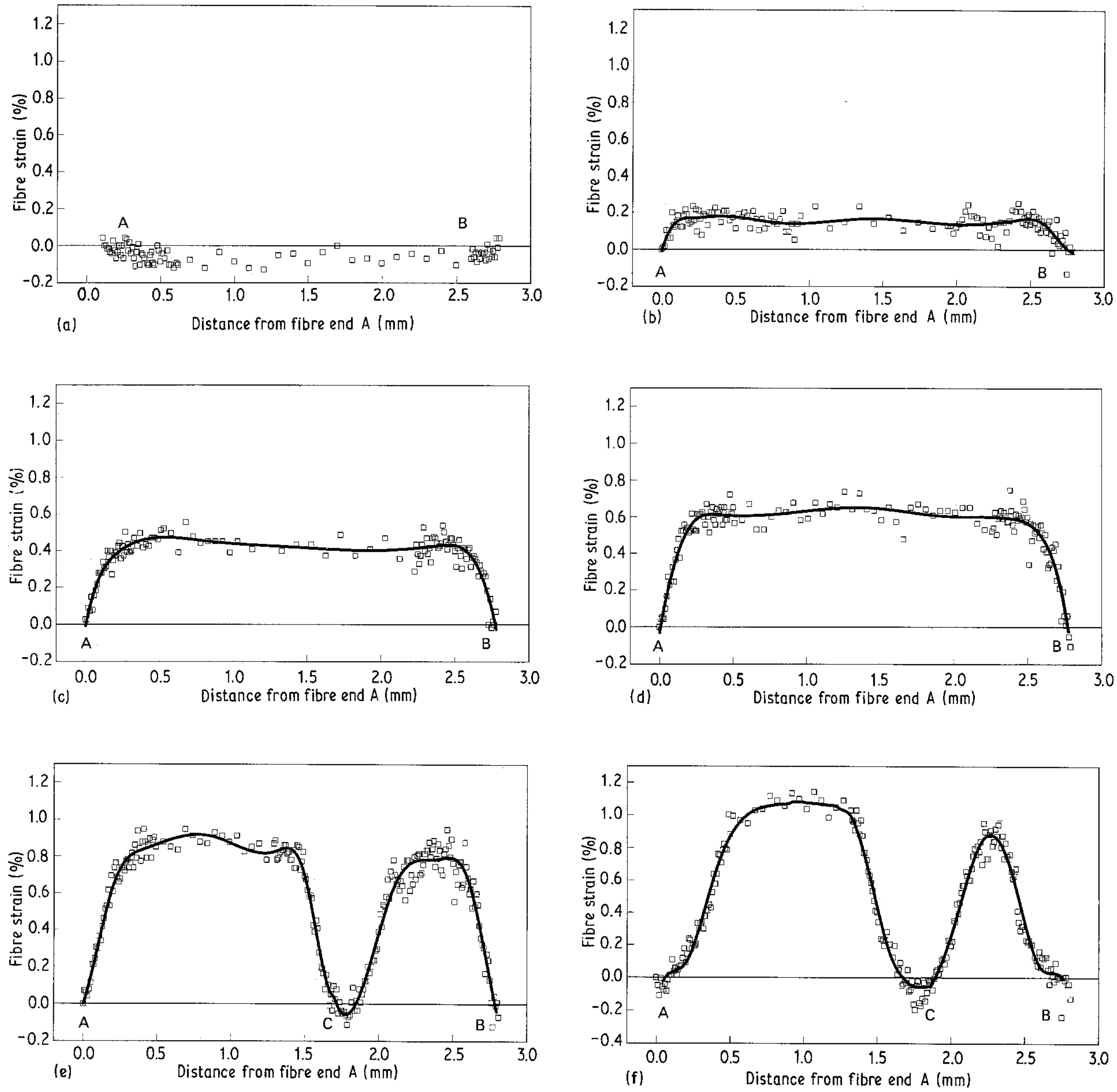

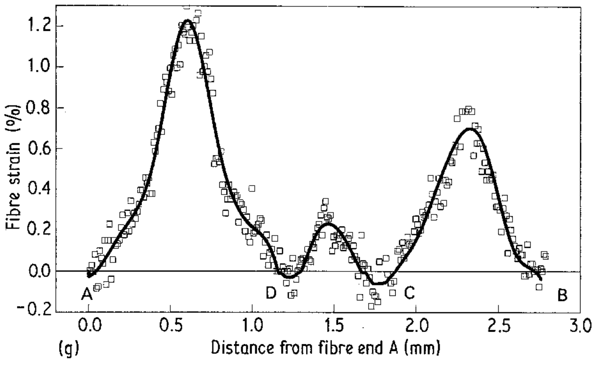

Figure 2 The fibre strain distribution along a short HMS fibre embedded in HY-1927 epoxy resin at applied strain of (a) 0.0%, (b) 0.2%, (c) 0.4%, (d) 0.6%, (e) 0.8%, (f) 1.0%, (g) 1.2%. (□) Experiment, (—) spline fit.

$\nu(i)$ by the expression:

$$\varepsilon_i = \frac{\nu(i) - \nu(0)}{\alpha_\varepsilon} \qquad (2)$$

where $\nu(0)$ is the frequency of stress-free fibre in air and α_ε is the Raman frequency gauge factor ($-11.4\ \mathrm{cm}^{-1}/\%$) for the G-line of the HMS fibre.

The strain profiles along the length of the short filament for seven distinct levels of applied strain, are shown in Fig. 2a–g. For clarity, the left- and right-hand ends of the fibre have been denoted A and B, respectively, while the fibre breaks have been denoted C and D. It can be seen that at 0.0% applied strain (Fig. 2a) the short fibre is under an initial compressive strain of about -0.05% as a result of resin shrinkage during curing. At 0.4% and 0.6% levels of applied strain, the fibre strain builds parabolically from the fibre ends and reaches a maximum value at the middle of the fibre. In general, this maximum value agrees reasonably well with the values of input strain as measured by means of a strain gauge glued to the surface of the resin block.

Fibre fracture occurs at 0.8% applied strain (Fig. 2e). The first fibre break C occurs at a distance of about 1.8 mm from A. The characteristic almost exponential type of axial strain take-up, indicates the presence of fibre/matrix debonding at the locus of the fibre break, as has been reported elsewhere [1]. It is interesting to note that at this point of incremental loading, the A and B profiles appear different from

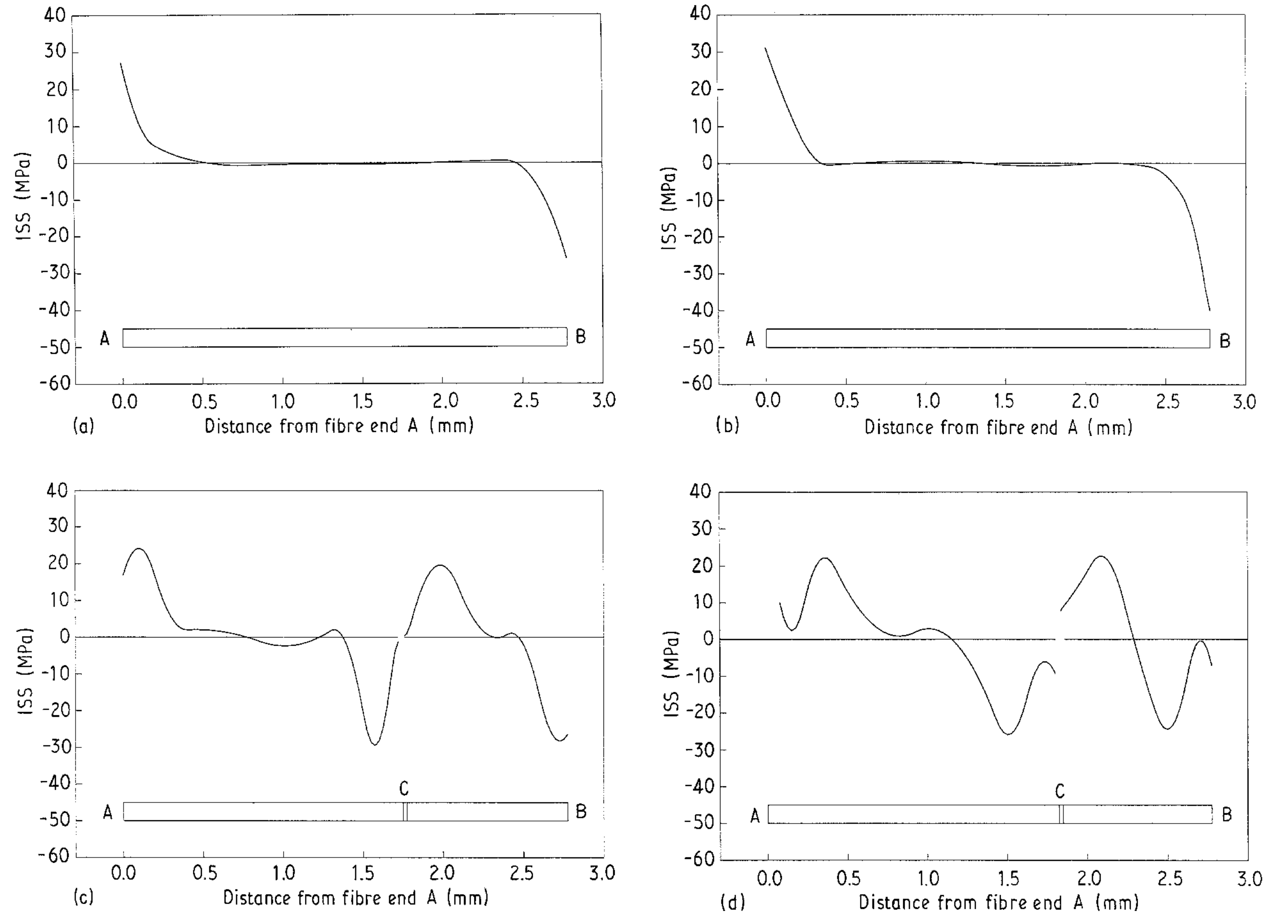

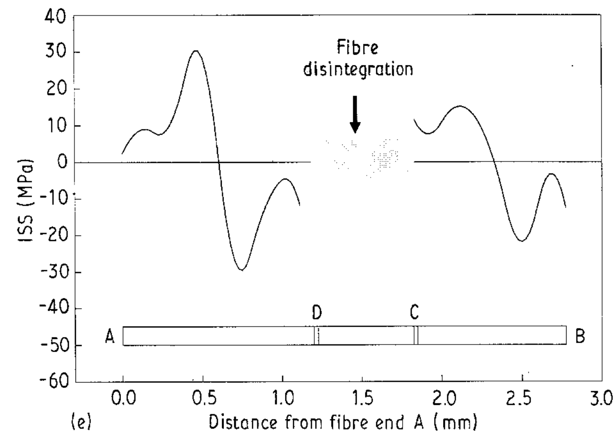

Figure 3 The interfacial shear stress distribution along the fibre at applied strains of (a) 0.4%, (b) 0.6%, (c) 0.8%, (d) 1.0% and (e) 1.2%. The ISS profiles were derived by (i) fitting a spline routine to the raw data, (ii) calculating the derivatives $d_{\varepsilon f}/dx$ from the equation of the best fit and, finally, (iii) deriving the ISS profiles by employing Equation 3.

those obtained at C, indicating that fibre/matrix debonding has not as yet initiated at the fibre ends. However, further increase of the applied strain to 1.0% (Fig. 2f), results in the transformation of the A and B profiles to the characteristic S-shape curves obtained at C. Further increase of the applied strain to 1.2%, brings about an additional fibre fracture at D (Fig. 2g) but the actual shape of the strain profiles remains unaffected.

3.3. Interfacial shear stress (ISS) distribution in the model composite

The interfacial shear stress distribution along the embedded fibre and its fragments is calculated from the fibre strain distribution by considering the balance of forces acting upon an infinitesimally small fibre element. This yields the following expression for the ISS

$$\tau(x) = E_f \frac{d}{4} \frac{\mathrm{d}\varepsilon(x)}{\mathrm{d}x} \tag{3}$$

where $\tau(x)$ is the interfacial shear stress (ISS) distribution along the fibre x-axis, E_f is the fibre modulus, d is the fibre diameter and $\varepsilon(x)$ is the fibre strain distribution along the fibre/fragment, as calculated in the previous stage. The functional representation of the fibre strain data can be derived through polynomial [1] or spline regression [4] of the individual experimental strain data. Both interpolations have been found to yield very similar results [20]. The applicability of this approach has been successfully demonstrated for a whole variety of fibre/resin systems [1–6].

The interfacial shear stress distribution has been calculated for the fibre strain profiles of Fig. 2c–g corresponding to applied strains of 0.4% to 1.2%. These ISS distributions have been obtained by means of a cubic spline regression and are shown in Fig. 3a–e. The position of fibre breaks at each level of applied strain, are also indicated in Fig. 3c–e. The maximum value of the ISS in each case, is displayed in Table II.

As can be seen in Fig. 3a and b, the ISS distributions at 0.4% and 0.6% applied strain reach a maximum value at the fibre ends A and B. This maximum starts

TABLE II Maximum ISS for the HMS/HY-1927 system

Profile	ISS_{max} (MPa) at applied strains shown					
	0.2%	0.4%	0.6%	0.8%	1.0%	1.2%
A	18.8	27.1	31.3	24.2	22.2	30.3
B	6.6	26.1	42.1	28.2	23.8	21.3
CA (break 1)				29.4	25.8	21.0
CB (break 1)				19.7	22.6	15.1
DA (break 2)						29.5
DB (break 2)						15.2
Average	12.6	26.6	36.7	25.4	23.6	20.4

to shift inwards along the fragment as the applied strain increases to 0.8% where the first fracture occurs at the middle of the fibre. However, the ISS distribution at the locus of fibre break is somewhat different; the ISS is zero at the fibre end and builds to a maximum value of about 26 MPa over a distance of about 15 fibre diameters. At the next increment of applied strain (1.0%, Fig. 3d), the ISS distribution obtained from the fibre ends A and B and the fibre break at C, are remarkably similar; the ISS fluctuates between zero and 10 MPa at the very tip of the fibre and then builds to a maximum value of not greater than 25 MPa over a distance of 40 fibre diameters. Finally, at an applied strain of 1.2% (Fig. 3e) where further fibre fragmentation occurs, three distinct regions can be clearly identified: (a) a region of ISS fluctuation around a constant quotient, (b) an area of ISS build-up to a maximum value and, finally, (c) a region of ISS decay to zero values.

The maximum ISS as a function of applied strain is shown in Fig. 4, for all strain profiles. The same set of results is also displayed in a tabulated form in Table II. As can be seen in Fig. 4, prior to fibre fracture, the average maximum ISS increases with applied strain to 35 MPa at 0.6% applied strain. This value compares well with the value of 37 MPa obtained from the HMS/MY-750 system [1] at higher applied strains employing a fragmentation test/geometry. After fibre fracture, the average maximum ISS relaxes to lower values forming a plateau at around 25 MPa.

4. Discussion

4.1. ISS distribution: theory and experiment

Analytical expressions describing the ISS distribution as a function of distance from the fibre end, have been derived by a number of authors [11–16]. According to Cox's shear-lag analysis [11], the ISS distribution is given by

$$\tau(x) = E_f \varepsilon \frac{G_m}{2E_f \ln(R/r)} \frac{\sinh \beta(L/2 - x)}{\cosh(\beta L/2)} \quad (4)$$

where E_f is the fibre modulus, ε is the applied strain, G_m is the matrix shear modulus, r is the radius of the fibre, R is the interfibre distance, L is the fibre length and $\beta = [2G_m/E_f r^2 \ln(R/r)]^{1/2}$.

Theoretical ISS curves derived from Equation 4, are shown in Fig. 5a–d for four different levels of applied strain (0.4%, 0.6%, 0.8% and 1.0%). These curves have been derived assuming that both constituents behave elastically and that there is perfect bonding between them. The characteristic ratio, R/r, for single-fibre model composites, can be taken as defining the limits of a cylindrical element beyond which the matrix extends freely under the influence of an external stress [5]. A value of $R/r = 5$ appears to give a reasonable estimate of the field of influence of the interphase upon the interfacial properties of the system [5, 21].

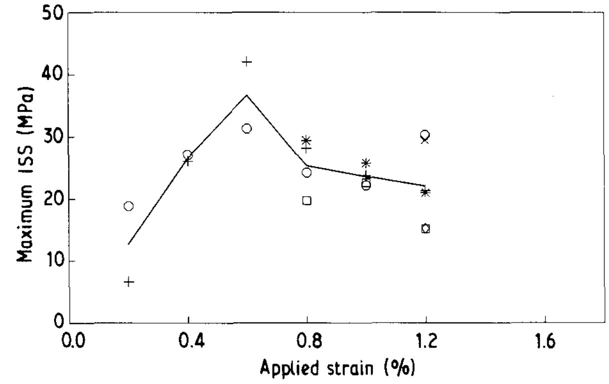

Figure 4 The maximum interfacial shear stress for the HMS/HY-1927 system, as a function of applied strain. Profile: (○) A, (+) B, (✱) CA, (□) CB, (×) DA, (◇) DB. (—) Average.

The experimentally derived ISS distributions are also plotted in Fig. 5a–d. As can be seen, good qualitative agreement between theory and experiment is obtained at 0.4% for the HMS/HY-1927 model composite. This again verifies the applicability of the shear-lag model for systems that have not been loaded beyond their elastic limit [5]. However significant deviations from the theoretical curves are observed at strains equal or higher than 0.8% (Fig. 5c and d) where interfacial failure is likely to have occurred; the system seems incapable of supporting any stresses higher than 35 MPa and the maximum value of ISS at 1.0% applied strain appears to have shifted 40 fibre diameters away from the fibre end. Because no higher shear stresses are allowed to develop, it can be safely assumed that the composite has now reached an upper limit of ISS or, in other words, its interfacial shear strength (IFSS).

4.2. The effect of interfacial failure upon the ISS distribution

It is now evident that interfacial failure is initiated at applied strains marginally lower than the lowest strain

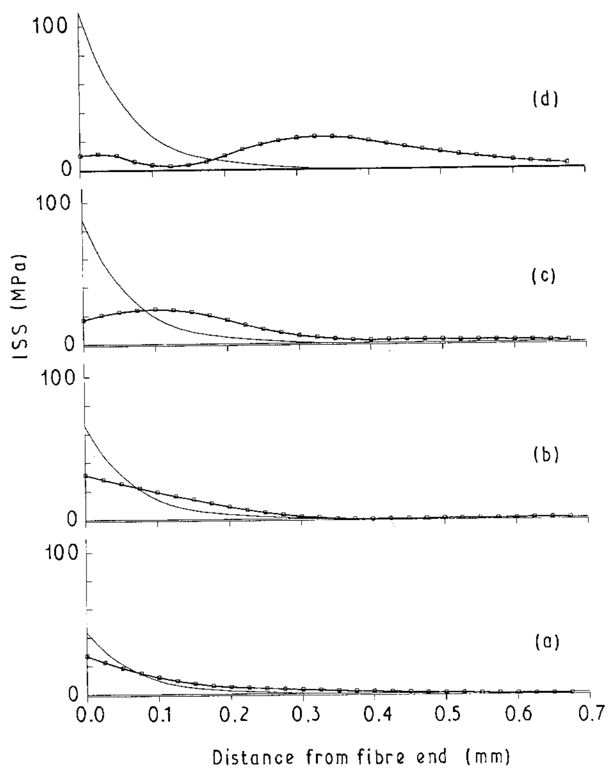

Figure 5 (–) The experimental interfacial shear stress distribution along the fibre end A of the HMS/HY-1927 system. (—) The theoretical prediction of the Cox model [11]; for a matrix/fibre ratio $R/r = 5$, at four levels of applied strain: (a) 0.4%, (b) 0.6% (c) 0.8% and (d) 1.0%.

required to fracture the fibre (0.8%). It follows that at the instant of fibre fracture in a fragmentation experiment on HMS/HY-1927 (or similar) systems, the interface at high applied strains (> 0.8%) has potentially reached its IFSS and, therefore, debonding is expected to propagate in an unstable manner. This is exactly what has been observed during tensile loading of continuous HMS/MY-750 model composites [1] and agrees well with a recent analysis by Piggott [22].

In Fig. 6, $\tau(x)$ is the function that describes the ISS distribution at the specific fibre/resin system and the IFSS "ceiling" represents the strength of the interfacial bond. At low applied strain, ε_1, the resulting ISS distribution, expressed by the function $\tau_1(x)$, does not intersect the IFSS line, allowing the maximum ISS to develop at, or very close to the fibre end. However, when the applied strain, ε_2, induces an ISS distribution, $\tau_2(x)$, which intersects the IFSS line, the region between the fibre end, $x = 0$, and the intersection point, $x = b$ (Fig. 6), is momentarily subjected to extremely high shear stresses, that exceed the interfacial shear strength of the system. This is the region where either the interphasial material is expected to yield, or the interfacial bonds to break. Clear interphasial yielding would result in a constant shear stress along the interphase of magnitude equal with its yield stress value [4]. However as is apparent from Fig. 3c–e, a gradual drop/relaxation of the ISS at the fibre ends is observed in the case of the HMS/HY-1927 system. This indicates that the interphase does not fail in a brittle manner but possesses a certain degree of ductility which manifests itself by the progressive rupture of individual chemical and/or physical fibre/matrix bonds. It is worth noting here that this gradual drop of ISS to zero value at the fibre tip, is always followed by the propagation of a Mode II interfacial crack regardless of the location of failure initiation (fibre end or break, Fig. 3c–e).

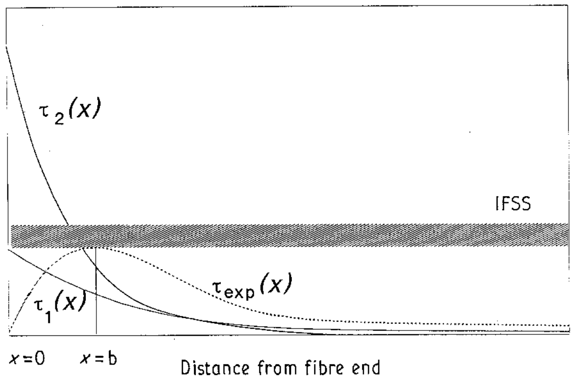

Figure 6 A schematic representation of the expected theoretical interfacial shear stress ISS distribution for a purely elastic system and the experimentally derived ISS distribution after initiation of interfacial failure. (—) The interfacial shear strength (IFSS) of the system. .

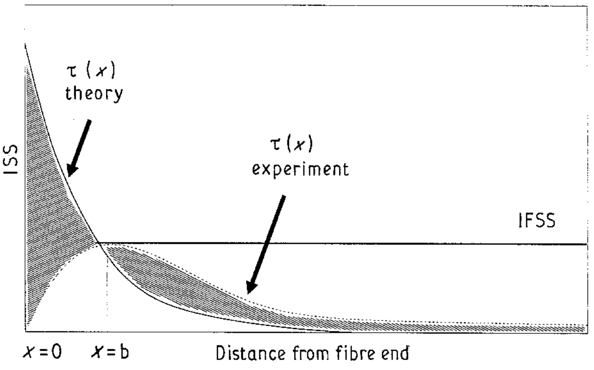

Figure 7 The maximum interfacial shear stress for the HMS/HY-1927 system, as a function of applied strain. The shaded areas before and after the intersection point ($x = b$) should be of equal size.

The region between thd fibre tip $x = 0$ and the intersection point $x = b$ (Fig. 6), is a region of gradually softened or partially debonded interface. The degree of "softening" should be proportional to the difference of the momentarily developed shear stress, $\tau_2(x)$, and the IFSS that the system can actually support. When the theoretically predicted maximum ISS just exceeds the IFSS, then a drop in the ISS values near the fibre end is observed (Fig. 3c). Further increase of the applied strain results in further reduction of the loading capability of the interface near the fibre end and minimization of the shear stress at this point (Fig. 3d and e).

Any weakening at the interface as a result of interfacial yielding or debonding, etc., should be counterbalanced by an increase of the shear energy transmitted to the system for the fibre to be effectively loaded. As shown schematically in Fig. 7, the shaded regions before and after the $x = b$ point should be equal, if the predicted maximum axial stress in the middle of the fibre is to be experimentally achieved. This explains why the shape of the resulting ISS

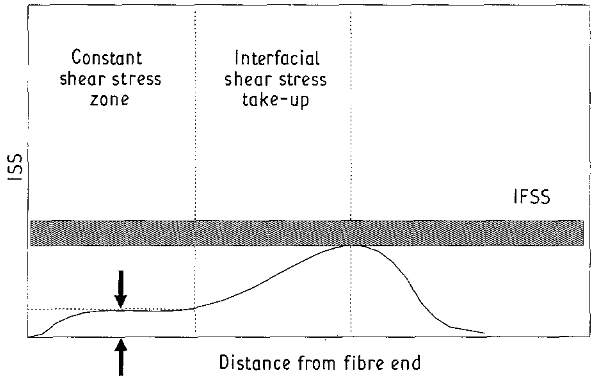

Figure 8 A schematic representation of the ISS distribution at high values of applied strain. The area of "constant" shear stress represents the debonded part of the fibre.

distribution at $x > b$, differs from the theoretical function $\tau(x)$.

The reduction of the ISS to zero values which is observed at the fibre break C at $\varepsilon = 0.8\%$ and at the fibre ends A and B at $\varepsilon = 1.0\%$, is a clear indication of the initiation of fibre/matrix debonding from existing discontinuities in the composite system. The fact that interfacial debonding at the fibre break precedes that at the fibre end is not surprising in view of the recoiling of the fibre as a result of fibre fracture and the associated release of strain energy [1]. However, what is demonstrated clearly here is the fact that fibre/matrix debonding is the preferred mode of interfacial failure in the HMS/HY-1927 systems, regardless of the nature of the discontinuity. This behaviour contrasts with certain aramid/epoxy model composites [4] for which pronounced interphasial plastic yielding rather than fibre/matrix debonding, is the observed mode of failure.

Once fibre/matrix debonding has been initiated and the shear stresses at this point are nearly zero, any additional increase to the applied strain results in the shifting of the whole ISS take-up region ($x = 0$–b) towards the middle the fibre/fragment as debonding propagates at the expense of the well-bonded length [1]. The development of shear stresses in the debonded area, is now the direct result of frictional forces the magnitude of which depends upon the morphology of the debonded region, the geometry of the propagating crack and the magnitude of the residual stresses due to resin curing. A schematic representation of the ISS profile at high applied strains, is shown in Fig. 8.

5. Conclusion

Laser Raman spectroscopy has been used to measure the strain along a short carbon fibre (HMS) embedded in a block of epoxy resin (HY-1927). By means of a balance of forces model, the fibre strain distribution has been converted to an interfacial shear stress distribution. It has been found that up to 0.8% of applied strain, the interfacial shear stress is maximum at the fibre ends and then decays rapidly to zero. The shape of the ISS profile is in agreement with shear lag type of approaches which assume perfect fibre/matrix adhesion. At 0.8% applied strain and beyond, the maximum ISS shifts away from the fibre end and drops in value. Similarly, the ISS profiles, obtained at the point of fibre fracture shows more extensive interfacial damage. At higher strains, three regions of (a) debonded (b) partially bonded and (c) well-bonded fibre, can be identified in the case of all ISS profiles, regardless of whether they are activated from a fibre end or a fibre break.

Acknowledgements

We thank the Defence Research Agency, the Department of Trade and Industry and the Science and Engineering Research Council for their financial contribution. Thanks are also due to Dr M. Pitkethly, DRA, for useful comments and discussions.

References

1. N. MELANITIS, C. GALIOTIS, P. L. TETLOW and C. K. L. DAVIES, *J. Compos. Mater.* **26** (1992) 574.
2. N. MELANITIS and C. GALIOTIS, *Proc Roy Soc. Ser. A* (1993) in press.
3. H. JAHANKHANI and C. GALIOTIS, *J. Compos. Mater.* **25** (1991) 609.
4. C. VLATTAS and C. GALIOTIS, in "Proceedings of ECCM-5," edited by A. R. Bunsell, Bordeaux 1992, pp. 415–20 E.A.C.M Bordeaux (1992).
5. C. GALIOTIS, *Compos. Sci. Technol.* **42** (1991) 125.
6. N. MELANITIS, P. L. TETLOW, C. GALIOTIS and C. K. L. DAVIES, in "Interfacial Phenomena in Composite Materials '89", edited by F. Jones, Sheffield (UK), (Butterworths, Oxford 1989) pp. 97–104.
7. A. KELLY, "Strong Solids" (Clarendon Press, Oxford, 1966).
8. W. A. FRASER, F. H. ANCKER and A. T. DIBENEDETTO, in "Conference Proceedings", 30th Annual Technical Conference on Reinforced Plastics (The Society of Plastics Industry, 1975) Section 22-A.
9. L. T. DRZAL, M. J. RICH and P. F. LLOYD, *J. Adhesion* **16** (1983) 1.
10. J. P. FAVRE and D. JACQUES, *J. Mater. Sci.* **25** (1990) 1373.
11. H. L. COX, *Brit. J. Appl. Phys.* **3** (1952) 72.
12. N. F. DOW, Report R63SD61, Space Sciences Laboratory, General Electric (1963).
13. C. C. CHAMIS, in "Composite Materials", Vol. 6 (Academic Press, New York, 1974) pp. 31–77.
14. W. WHITNEY and L. T. DRZAL, (1987), in "Toughened Composites", ASTM STP 937, edited by N. Johnston, (American Society for Testing and Materials, Philadelphia, 1987) pp. 179–96.
15. L. N. McCARTNEY, National Physical Laboratory Report DMA(A) 168, (1988).
16. A. N. NETRAVALI, R. B. HENSTENBURG, S. L. PHOENIX and P. SWHWARTZ, *Polym. Compos.* **10** (1989) 226.
17. F. TUINSTRA and J. KOENIG, *J. Chem. Phys.* **53** (1970) 1126.
18. M. GUIGON, A. OBERLIN and G. DESARMOT, *Fibre Sci. Technol.* **20** (1984) 177.
19. M. S. DRESSELHAUS, G. DRESSELHAUS, K. SUGIHARA, I. L. SPAIN and H. A. GOLDBERG, in "Graphite Fibres and Filaments" (Springer-Verlag, Berlin, 1988).
20. N. MELANITIS, PhD thesis, University of London (1991).
21. G. P. CHEREPANOV, in "Mechanics of Brittle Fracture" (McGraw-Hill, New York, 1979) Ch. 9.
22. M. R. PIGGOTT, *Compos. Sci. Technol.* **42** (1990) 57.

Received 1 July
and accepted 24 July 1992